

Analysis and data-based modeling of the photochemical reaction dynamics of the induced singlet oxygen in light therapies

Wang, Tianfeng ; Dong, Jianfei; Zhang, Guoqi

DOI

[10.1109/TBME.2022.3170541](https://doi.org/10.1109/TBME.2022.3170541)

Publication date

2022

Document Version

Final published version

Published in

IEEE Transactions on Biomedical Engineering

Citation (APA)

Wang, T., Dong, J., & Zhang, G. (2022). Analysis and data-based modeling of the photochemical reaction dynamics of the induced singlet oxygen in light therapies. *IEEE Transactions on Biomedical Engineering*, 69(11), 3427-3437. Article 9763299. <https://doi.org/10.1109/TBME.2022.3170541>

Important note

To cite this publication, please use the final published version (if applicable).
Please check the document version above.

Copyright

Other than for strictly personal use, it is not permitted to download, forward or distribute the text or part of it, without the consent of the author(s) and/or copyright holder(s), unless the work is under an open content license such as Creative Commons.

Takedown policy

Please contact us and provide details if you believe this document breaches copyrights.
We will remove access to the work immediately and investigate your claim.

Green Open Access added to TU Delft Institutional Repository

'You share, we take care!' - Taverne project

<https://www.openaccess.nl/en/you-share-we-take-care>

Otherwise as indicated in the copyright section: the publisher is the copyright holder of this work and the author uses the Dutch legislation to make this work public.

Analysis and Data-Based Modeling of the Photochemical Reaction Dynamics of the Induced Singlet Oxygen in Light Therapies

Tianfeng Wang^{1b}, Jianfei Dong^{1b}, and Guoqi Zhang, *Fellow, IEEE*

Abstract—Objective: The macroscopic singlet oxygen (MSO) model for quantifying the light-induced singlet oxygen (1O_2) always contain a set of nonlinear dynamic equations and therefore are generally difficult to be applied. This work was devoted to analyze and simplify this dynamic model. **Methods:** Firstly, the nonlinearity of the MSO model was analyzed with control theory. The conditions, under which it can be simplified to a linear one, were derived. Secondly, in the case of ample triplet oxygen concentration, a closed-form exact solution of the 1O_2 model was further derived, in a nonlinear algebraic form with only four parameters that can be easily fitted to experimental data. Finally, *in vitro* experiments of anti-fungal light therapies were conducted, where the fungi, *Candida albicans*, were irradiated respectively by the 385, 405, 415, and 450 nm wavelength light. The singlet oxygen concentration levels in the fungi were measured, and then used to fit the developed models. **Results:** The parameters of the closed-form exact solution were estimated from both the simulated and the measured experimental data. Based on this model, a functional relationship between the photon energy, fluence rate and singlet oxygen concentration was also established. The fitting accuracy of this model to the data was satisfactory, which therefore demonstrates the effectiveness of the proposed modeling techniques. **Conclusion:** The results from simulating the closed-form model indicate that the photon energy within the range of either 2.7 ~ 2.8 eV or 3.0 ~ 3.2 eV (388 ~ 413 nm or 443 ~ 459 nm in wavelength) is more effective in generating singlet oxygen in the fungi studied in this work. **Significance:** It is the first attempt of applying control theory to analyze the photochemical reaction dynamics of light therapies in terms of their nonlinearity. The proposed modeling techniques also offer opportunities for determining the light dosages in treating fungal infection diseases, especially those on the surface tissues of human body.

Manuscript received 27 January 2022; revised 24 March 2022; accepted 22 April 2022. Date of publication 26 April 2022; date of current version 20 October 2022. This work was supported in part by the National Natural Science Foundation of China under Grant 61873263 and in part by the Fundamental Research Project Fund of Suzhou under Grant SJC2021020. (Corresponding author: Jianfei Dong.)

Tianfeng Wang is with the Suzhou Institute of Biomedical Engineering and Technology, Chinese Academy of Sciences, China, and also with the Department of Microelectronics, Delft University of Technology, The Netherlands.

Jianfei Dong is with the Suzhou Institute of Biomedical Engineering and Technology, Chinese Academy of Sciences, Suzhou 215163, China (e-mail: jfeidong@hotmail.com).

Guoqi Zhang is with the Department of Microelectronics, Delft University of Technology, The Netherlands.

Digital Object Identifier 10.1109/TBME.2022.3170541

Index Terms—Low-level light therapy, reactive oxygen species, nonlinear dynamics, Mycoses.

I. INTRODUCTION

PHOTODYNAMIC therapies (PDT) have been investigated as non-antibiotic alternatives for treating localized infectious diseases due to their rapid action and lack of drug resistance [1], [2]. Similar to PDT, blue light therapies that rely only on the endogenous pigments, i.e., porphyrins and flavins, of the pathogens are also effective and even safer to use. The inactivation effect of blue light has been proven on the Gram-positive/negative bacteria [3], mycobacterium [4], and algae [5]. Likewise, anti-fungal blue light (ABL) has been widely studied as a new treatment approach of fungal infections. For instance, the effect of 415 nm LED light on *C. albicans* was studied and verified both *in vitro* and *in vivo* [6]. Blue light at 405 nm was also previously shown to be effective in reducing the seeding of exposed biofilms [7].

As a widely accepted hypothesis, the mechanisms of the anti-fungal effect of PDT and ABL are that the photons from light can excite either the exogenous photosensitizer (PS) in the former case or the endogenous pigments in the latter, which in turn produces reactive oxygen species (ROS) that affect cells [8], [9]. ROS are highly reactive chemical molecules formed due to the electron acceptability of O_2 . Examples of ROS include peroxides, superoxide, hydroxyl radicals, singlet oxygen [10], and alpha-oxygen [11]. According to a previous study [12], singlet oxygen usually accounts for 80% of all the ROS induced by light; while hydroxyl radicals and other types of ROS take the remaining 20%. Furthermore, singlet oxygen is a precursor of most other ROS, and it also becomes involved in the propagation of oxidative chain reactions [13].

Thus, there is greater interest in the quantum yield of singlet oxygen, whose cumulative dose has been used to determine the tissue damage caused by PDT [14]–[16]. Based on the mechanism of PDT, some first-principle models have been proposed to explore the dynamic changes in singlet oxygen concentration [17]–[19], which are highly nonlinear models. A set of coupled differential equations was used to describe this nonlinear process, including seven Michaelis-Menten-type equations corresponding to seven different state variables [19], i.e., the concentration of PS and various types of oxygen and the ROS acceptors excluding the PS molecules. Moreover, Monte

Carlo simulations were also combined with these types of kinetic models, and were proven to be effective in simulating the light transport in biological tissues [20]–[22].

These first-principle models can precisely fit the dynamic changes in the singlet oxygen concentrations. However, the parameters are related to the PS characteristics, and they should be determined from dedicated experiments. For instance, in a previous study [23], up to 21 parameters were required to describe the process related to the PS. A classical macroscopic time-scale singlet oxygen (MSO) model [18], [19] was simplified into three differential equations [21], [22] with some reasonable assumptions according to the reality. However, 6 parameters and 3 states remained. This simplified model was verified in a previous study [24], in which the concentrations of PS and triplet oxygen concentration were measured. The parameters were taken as the empirical values because of the difficulty in re-estimating them. However, although ABL are believed to be caused by the PSs that naturally exist in fungal cells, whose types and amounts are usually unknown, modeling by first-principles becomes even more challenging than modeling PDT. To accommodate these modeling challenges, data-driven modeling methods based on time-series have been investigated [25]–[27]. However, there is still no attempt made to ease the model form and the parameter estimation in the classical MSO models, in a similar data-driven fashion based on measured time-series data.

In this study, we first examined the nonlinear dynamics of the MSO model, and then analyzed the conditions under which it can be approximated by a linear model. Based on the standard system linearization method, a linearized model was developed and applied to simulate the concentration of singlet oxygen. We subsequently solved the differential equations in the MSO model for the case of an abundant oxygen supply, and obtained an analytical solution of the concentration of singlet oxygen. In experiments, the singlet oxygen levels are measured from *C. albicans* under the irradiation of four LED light sources with wavelengths of 385, 405, 415, and 450 nm up to 30 minutes. Here, we chose *C. albicans* to study because it is one of the most common fungal pathogens [28], and it always infects membranes such as those of the mouth, vagina, and intestines in humans [29], [30]. The fitting accuracy of the analytical solution of the MSO model to the measured singlet oxygen concentrations also turned out to be satisfactory.

II. METHODS

A. Modeling Methods

1) Preliminaries of the First-Principle Model: A classical macroscopic time-scale singlet oxygen (MSO) model is based on the mechanism of PDT with the included rate equations

in Michaelis-Menten form [18], [19]. With some reasonable assumptions according to the reality, this model can be simplified into three differential equations [21], [22].

$$\frac{d[S_0]}{dt} = -\xi\sigma\frac{\phi([S_0] + \delta)[^3O_2]}{[^3O_2] + \beta}[S_0] \quad (1a)$$

$$\frac{d[^3O_2]}{dt} = -\xi\frac{\phi[S_0][^3O_2]}{[^3O_2] + \beta} + g \cdot \left(1 - \frac{[^3O_2]}{[^3O_2]_0}\right) \quad (1b)$$

$$\frac{d[^1O_2]}{dt} = f \cdot \xi\frac{\phi[S_0][^3O_2]}{[^3O_2] + \beta} \quad (1c)$$

where $[S_0]$ denotes the concentration of PS; $[^3O_2]$, $[^1O_2]$ denote the concentration of triplet and singlet oxygen, respectively; and $[^3O_2]_0$ denotes the initial concentration of triplet oxygen. The included parameters are light fluence rate ϕ [mW], specific oxygen consumption rate ξ [cm²/mW/s], the specific photobleaching ratio σ [μM^{-1}], the oxygen quenching threshold β [μM], the low concentration correction δ [μM], the fraction of 1O_2 interacting with target f , and the oxygen supply rate g [$\mu\text{M/s}$]. In an ample oxygen supply, the fraction f can be set as 1. Let g to be the external input, the nonlinearity of model (1) can be examined by the poles and zeros of its linearized model at different equilibrium points. If $\mathbf{x} = [[S_0] \ [^3O_2] \ [^1O_2]]^T$ is denoted as the state vector, and $u = g$ as the control input of the nonlinear system, then (1) can be rewritten in a state space form as

$$\frac{d\mathbf{x}}{dt} = h(\mathbf{x}, u), \quad (2)$$

where $h(\cdot)$ is a nonlinear vector-valued function.

2) Analysis of the First-Principle Model of PDT: To analyze (1), first note that if a nonlinear system operates around an equilibrium point, i.e. around a configuration where the system is at rest, then it is possible to study the behavior of the system in the neighborhood of such a point, where its dynamics can be reasonably approximated as a linear model. Based on the standard linearization method of a nonlinear system [31], we can linearize (2) as

$$\frac{d\mathbf{x}}{dt} = \mathbf{A}\mathbf{x} + \mathbf{B}u, \quad (3)$$

where \mathbf{A} is defined as $\mathbf{A} = \left. \frac{\partial h}{\partial \mathbf{x}} \right|_{\mathbf{x}^*, u^*}$; \mathbf{B} is defined as $\mathbf{B} = \left. \frac{\partial h}{\partial u} \right|_{\mathbf{x}^*, u^*}$; and \mathbf{x}^*, u^* denotes an equilibrium point. Thus, the linearized matrices \mathbf{A} and \mathbf{B} can be expressed as (4), shown at the bottom of the page, and (5).

$$\mathbf{B} = [0 \quad 1 - [^3O_2]/[^3O_2]_0 \quad 0]^T \quad (5)$$

Because the main objective is to model and track the concentration of 1O_2 , an output equation can be added to (3), which

$$\mathbf{A} = \begin{bmatrix} -\xi\sigma\phi\frac{[^3O_2]}{[^3O_2] + \beta}(2[S_0] + \delta) & -\xi\sigma\phi([S_0] + \delta)[S_0]\left(\frac{1}{\beta + [^3O_2]} - \frac{[^3O_2]}{(\beta + [^3O_2])^2}\right) & 0 \\ -\xi\phi\frac{[^3O_2]}{[^3O_2] + \beta} & -g/[^3O_2]_0 - \xi\phi[S_0]\left(\frac{1}{\beta + [^3O_2]} - \frac{[^3O_2]}{(\beta + [^3O_2])^2}\right) & 0 \\ f\xi\phi\frac{[^3O_2]}{[^3O_2] + \beta} & f\xi\phi[S_0]\left(\frac{1}{\beta + [^3O_2]} - \frac{[^3O_2]}{(\beta + [^3O_2])^2}\right) & 0 \end{bmatrix} \quad (4)$$

leading to a standard state-space form:

$$\frac{d\mathbf{x}}{dt} = \mathbf{A}\mathbf{x} + \mathbf{B}u \quad (6a)$$

$$\mathbf{y} = \mathbf{C}\mathbf{x}. \quad (6b)$$

Here, as a reminder, the state vector is $\mathbf{x} = [[S_0] [^3O_2] [^1O_2]]^T$. The output matrix $\mathbf{C} = [0 \ 0 \ 1]$, since the third dimension of the state vector is $[^1O_2]$.

To examine the level of the nonlinearity of this dynamic process, one can study the variation of the poles at different equilibrium points. It is well known in the control theory literature that the poles and zeros of a system determine its dynamic behavior in response to exogenous stimuli [31]. First, note that for the state-space model (3), the poles are the eigenvalues of system matrix \mathbf{A} [31], which are denoted as λ . Because $\mathbf{A} \in \mathbb{R}^{3 \times 3}$, it has three eigenvalues. Based on the standard linear algebra, one eigenvalue is 0, because the third column of \mathbf{A} are all 0's; while the other two can be obtained by solving the following characteristic equation:

$$(\lambda - a_{11})(\lambda - a_{22}) - a_{12} \cdot a_{21} = 0, \quad (7)$$

where a_{ij} denotes the element on the i -th row and j -th column of \mathbf{A} . Therefore, three eigenvalues can be written as:

$$\begin{aligned} \lambda_1 &= 0 \\ \lambda_2 &= \frac{1}{2} \left[a_{11} + a_{22} - \sqrt{(a_{11} + a_{22})^2 - 4(a_{11} \cdot a_{22} - a_{12} \cdot a_{21})} \right] \\ \lambda_3 &= \frac{1}{2} \left[a_{11} + a_{22} + \sqrt{(a_{11} + a_{22})^2 - 4(a_{11} \cdot a_{22} - a_{12} \cdot a_{21})} \right]. \end{aligned}$$

Under the real conditions of photofrin-mediated PDT [21], [22], the term σ is far less than the other parameters, i.e., $\sigma = 9 \cdot 10^{-5} \mu\text{M}^{-1}$, $\xi = 3.7 \cdot 10^{-3} \text{ cm}^2/\text{mW/s}$, $\delta = 33 \mu\text{M}$, $\beta = 11.9 \mu\text{M}$. This leads to $a_{11}, a_{12} \approx 0$, which contains σ . Thus, the term $a_{11} \cdot a_{22} - a_{12} \cdot a_{21} \approx 0$. After substituting this into the equation above, the eigenvalues can be simplified to

$$\begin{cases} \lambda_1 = 0 \\ \lambda_2 \approx 0 \\ \lambda_3 \approx a_{11} + a_{22} \end{cases}. \quad (8)$$

Obviously, there is a pole at the origin (λ_1) and two negative real poles. However, the analytic solutions of the zeroes are not as straightforward as those of the poles. Whereas, according to the simulation results to be presented later, the linearized models only contain one zero. Therefore, the linearized model can also be written in a transfer function form, i.e.,

$$H(s) = K \cdot \frac{s - z}{s(s - \lambda_2)(s - \lambda_3)} \quad (9)$$

$$\approx \frac{K}{(s - \lambda_2)(s - \lambda_3)}, \quad (10)$$

where K and z are respectively the gain and zero. According to the simulations to be presented later, the order of magnitude of z is only -5 in all the linearized systems. This trivial zero always cancels the pole at the origin, which approximately leads to a second order transfer function (10) by standard minimal realization theory. This will also be illustrated in the root-locus plots of the linearized systems at different equilibrium points in

Section III-A. Consequently, the transfer function (10) contains a dominant pole (λ_2) and a non-dominant one (λ_3).

Based on the locations of the zero and poles of the linearized systems, we mainly need to analyze λ_2 and λ_3 . Besides, due to the simpler form of λ_3 , we will now focus on analyzing λ_3 to investigate the nonlinearity of the MSO process. First, substituting the corresponding terms of (4) into λ_3 as follows, we obtain:

$$\lambda_3 = -\xi\sigma\phi \frac{[^3O_2](2[S_0] + \delta)}{[^3O_2] + \beta} - \frac{g}{[^3O_2]_0} - \frac{\xi\phi\beta[S_0]}{(\beta + [^3O_2])^2} \quad (11)$$

Here, λ_3 is a negative real pole, which defines an exponentially decaying component in the dynamic response, i.e., $e^{\lambda_3 t}$. In this MSO model, the initial concentration of triplet oxygen and the oxygen supply rate can be artificially adjusted by the oxygen content of the environment where the cells are exposed. If the external environment is oxygen-rich, one can expect that the concentration of triplet oxygen, i.e., $[^3O_2]$, is far greater than β , and thus, the limit of λ_3 is simplified to:

$$\lim_{[^3O_2] \rightarrow +\infty} \lambda_3 = -\xi\sigma\phi(2[S_0] + \delta) \quad (12)$$

Because ξ , σ , and ϕ are constant parameters, the concentration of PS, i.e., $[S_0]$, becomes the only factor that can change the third pole, which in turn affects the dynamic response of the system. As will be detailed later in the simulation results, there is actually little change in $[S_0]$ during the whole process. Thus, the limit (12) is approximately a constant. Similarly, the same conclusion can be drawn on $\lim_{[^3O_2] \rightarrow +\infty} \lambda_2$, which are also supported by the simulation results in Section III-A.

Taking into account that λ_2 and λ_3 are approximately constants, the MSO model can thus be approximated by a linear time invariant model, in the case of abundant oxygen supply. Thus, one can use the linearized model (6) to simulate the concentration of light-induced singlet oxygen $[^1O_2]$.

It is worth mentioning that the linearized model (6) is a second-order linear-time-invariant (LTI) model after the pole-zero cancelation, containing two poles. In comparison, another LTI model [26] is a first-order model with only one pole, whose value is close to the dominant pole λ_2 .

3) Analytical Solution of $[^1O_2]$ With Abundant 3O_2 : Although the approximated linear model (6) provides additional insights into the dynamic behavior of the MSO process, it can also lead to large prediction errors in the long-term trajectories of $[^1O_2]$ due to the approximations made for both the zeros and poles. This further motivates the derivation of an exact solution of the differential equations in (1), in the case of abundant 3O_2 .

Based on the situation of the abundant oxygen supply, $[^3O_2]$ is much greater than β . With this condition, $\frac{[^3O_2]}{[^3O_2] + \beta}$ can approximate to a constant as

$$\lim_{[^3O_2] \rightarrow +\infty} \frac{[^3O_2]}{[^3O_2] + \beta} = 1. \quad (13)$$

It is difficult to derive a closed-form solution of $[^1O_2]$ from the linearized model of (3), which contains three states. Neglecting the variation in the concentration of 3O_2 and the approximation

in (13), we can eliminate (1b) and derive the following second-order dynamics:

$$\frac{d[S_0]}{dt} = a([S_0] + \delta)[S_0] \quad (14a)$$

$$\frac{d[{}^1O_2]}{dt} = c[S_0] \quad (14b)$$

where $a = -\xi\sigma\phi$ and $c = f \cdot \xi\phi$. Note that, one of the two poles of (14) is exactly the same as that in (12); another pole was at the origin.

Then, (14a) can be solved as follows:

$$\frac{1}{a([S_0] + \delta)[S_0]} d[S_0] = dt \quad (15a)$$

$$\frac{1}{a\delta} \left(\frac{1}{[S_0]} - \frac{1}{([S_0] + \delta)} \right) d[S_0] = dt \quad (15b)$$

Integrating both sides simultaneously leads to:

$$\frac{1}{a\delta} (\ln[S_0] - \ln([S_0] + \delta)) = t + C_1 \quad (16a)$$

$$[S_0] = \frac{\delta e^{a\delta(t+C_1)}}{1 - e^{a\delta(t+C_1)}} \Rightarrow C_1 = \frac{\ln \frac{[S_0]_0}{[S_0]_0 + \delta}}{a\delta} \quad (16b)$$

where C_1 denotes the constant corresponding to the initial state of $[S_0]$, denoted as $[S_0]_0$.

Finally, after substituting (16b) into (14b), the following analytical solution of $[{}^1O_2]$ can be derived as:

$$\frac{d[{}^1O_2]}{dt} = c \frac{\delta e^{a\delta(t+C_1)}}{1 - e^{a\delta(t+C_1)}} \quad (17a)$$

$$[{}^1O_2] = -\frac{c}{a} \ln(1 - e^{a\delta(t+C_1)}) + C_2 \quad (17b)$$

$$C_2 = \frac{c}{a} \ln(1 - e^{a\delta C_1}) \quad (17c)$$

where C_2 is a constant offset to ensure the initial value of $[{}^1O_2]$, i.e., the induced singlet oxygen by light at $t = 0$, to be zero. For the simplicity of the notations, denote $k_1 = -\frac{c}{a}$, $k_2 = e^{a\delta C_1}$, $k_3 = -\frac{a}{\delta}$, $k_4 = C_2$. According to the definitions of a and c in (14), and C_1 in (16b), the parameters k_1 , k_2 , and k_3 actually take the following forms:

$$k_1 = \frac{f}{\sigma}, k_2 = e^{\ln \frac{[S_0]_0}{[S_0]_0 + \delta}}, k_3 = \xi\sigma\delta.$$

Now, (17b) can be finally written as:

$$[{}^1O_2] = k_1 \ln(1 - k_2 e^{-\phi k_3 t}) + k_4, \quad (18)$$

which is an analytical solution of $[{}^1O_2]$ in (1) in the case of abundant 3O_2 . Note that although $k_1 \sim k_4$ are determined by the original parameters $[S_0]_0$, σ , δ , ξ , and f , fitting (18) actually does not require knowing or estimating these original ones. Therefore, only four parameters (k_1 , k_2 , k_3 , and k_4) need to be estimated to fully know (18).

4) Functional Relationship Between k_3 and Photon Energy: In classical PDT models, the PDT dose is defined as the number of photons absorbed by the PS, and is related to the fluence rate and the photon energy. The kinetic PDT equations

are henceforth parameterized by the fluence rate and photon energy of the stimulating light.

The energy of a photon is inversely proportional to the wavelength of the light, which is usually given in the unit of electron-volt (eV), i.e.:

$$E_p = \frac{hc}{\lambda} \quad (19)$$

where h and c denote the Planck's constant and the speed of light, respectively. Here, the unit of λ shall be converted from nanometers to microns. Photon energy will also be used to quantify a specific light source, as follows.

In (18), k_3 is the only parameter related to ξ , which is anti-proportional to the photon energy. Thus, the functional relationship between k_3 and E_p can be established as follows.

Based on our acknowledgments, the main PSs in *C. albicans* are flavin and porphyrin, whose peak absorptions are at 405 nm and 460 nm, respectively. Thus, the blue light of these two wavelengths can effectively inhibit the *C. albicans*. Moreover, k_3 is a parameter that reflects the singlet oxygen accumulation speed, which is correlated with the inhibition. Here, we use a piecewise function in (20) to describe this dependence of k_3 on the photon energy:

$$k_3 = \begin{cases} a_1 + b_1 \cdot \sin(c_1 E_p + d_1), & E_p \leq \bar{E} \\ a_2 + b_2 \cdot \sin(c_2 E_p + d_2), & E_p > \bar{E} \end{cases} \quad (20)$$

where $a_1, a_2, b_1, b_2, c_1, c_2, d_1, d_2$ are the parameters to be estimated; and \bar{E} is demarcation point of the piecewise function that describes the peak near 415 nm or 460 nm.

5) Modeling $[{}^1O_2]$ as a Function of Photon Energy and Fluence Rate: Now, by substituting (20) into (18) and noting that $\phi \cdot t = H_e$ (i.e., assuming a constant fluence rate), the model of the 1O_2 concentration y as a function of the photon energy and fluence can be finally derived in (21).

$$y(H_e, E_p) = \begin{cases} k_1 \ln(1 - k_2 e^{-[a_1 + b_1 \cdot \sin(c_1 E_p + d_1)] H_e}) \\ \quad + k_4, & E_p \leq \bar{E} \\ k_1 \ln(1 - k_2 e^{-[a_2 + b_2 \cdot \sin(c_2 E_p + d_2)] H_e}) \\ \quad + k_4, & E_p > \bar{E} \end{cases} \quad (21)$$

Therefore, the 1O_2 concentration can be calculated using the photon energy and fluence rate of a treatment light source. This model can be applied in analyzing and calculating light dosages in clinical PDTs and ABLs. However, the fluence rate is found in clinical and *in-vivo* experiments to be highly subject to the optical properties of various tissues and the light wavelength [32]. In this study, we will especially focus on analyzing the light fluence rate in the superficial tissues of human body in what follows.

6) Fluence Rate for Treating Fungal Infections in Cutaneous Tissues: For fungal infections in cutaneous tissues, i.e., on the surface of human body, external treatment light can be effectively applied to the skin. As a common practice in the literature [22], [32], a shallow layer of the skin tissue can be assumed as a semi-infinite medium with uniform optical properties, i.e., with the same absorption coefficient μ_a and the same reduced scattering coefficient μ'_s . On the other hand,

for a planar light source that is applied externally, due to the backscattering effect from the tissue-air boundary, the fluence rate beyond the boundary in the tissue can be even greater than that in the air [32]. That is

$$\frac{\phi}{\phi_{air}} = 1 + 2R_d, \quad (22)$$

where ϕ_{air} is the fluence rate of the incident light. R_d is the diffuse reflectance, and can be calculated as [32]:

$$R_d = \frac{a'}{2} \left(1 + e^{-\frac{4/3}{A} \sqrt{3(1-a')}} \right) \cdot e^{-\sqrt{3(1-a')}}, \quad (23)$$

where $a' = \mu'_s / (\mu_a + \mu'_s)$ is the transport albedo; A is a constant that can be calculated based on the index of the refractions of the tissue and air at the boundary. For an air-tissue interface, $A = 2.9$ is a good approximation [22], [33]. For estimating the light fluence rate within the tissue, the following Lambert's relationship is used.

$$\phi(d) = \phi_{air} \cdot k \cdot e^{-\mu_{eff} \cdot d}, \quad (24)$$

where d is the depth below the tissue; μ_{eff} is the effective attenuation coefficient, which can be calculated as $\mu_{eff} = \sqrt{3 \cdot \mu_a (\mu_a + \mu'_s)}$; and k is the backscatter coefficient, which is determined by [34] $k = 3 + 5.1R_d - 2e^{-9.7R_d}$.

The equations (22–24) suffice to characterize the light fluence rate in the cutaneous tissues below the air-skin boundary with a planar light source.

B. Experimental Methods

1) Chemicals and Materials: The growth medium was tryptic soy broth (TSB), and was purchased from Hopebiol (Qingdao, China). The test assay of 1O_2 was Singlet Oxygen Sensor Green (SOSG) reagent (Invitrogen, Eugene, USA), which was dissolved in methanol (100 μg in 33 μl) to create a stock solution of 5 mM.

2) Fungal Strains: The *C. albicans* used in this work is the 3147 (IFO 1594) strain (ATCC, Manassas, VA, USA). The fungal strain was cultured overnight in TSB at 26°C with shaking at 180 RPM. To maintain the concentration of the fungal suspension within the same range, the absorption of the suspension at 550 nm was measured by a U-3900H spectrophotometer (Hitachi, Tokyo, Japan) before all the experiments. More specifically, the absorption levels measured by this equipment were always controlled in the range of 2.3 ~ 2.5, which corresponds to a fungal density of 10^7 CFU/ml.

3) LED Light Source: Four different types of LEDs with specified peak wavelengths at 385, 405, 415, and 450 nm were selected to build four light sources. The spectral power density (SPD) curves for the LEDs, as measured by a Maya 2000 Pro spectrometer (Ocean Optics, Gloucester, MA, USA), are depicted in Fig. 1. In this figure, every SPD curve has been normalized with respect to its integral.

All the four light sources were made of a 4-by-4 LED array, arranged in a 1.5-by-1.5 cm square as previously described [26]. Every light source was able to provide a round spot with 15 cm diameter at 10 cm height above the sample. The target fluence rate in all the experiments was 50 mW/cm². The distribution

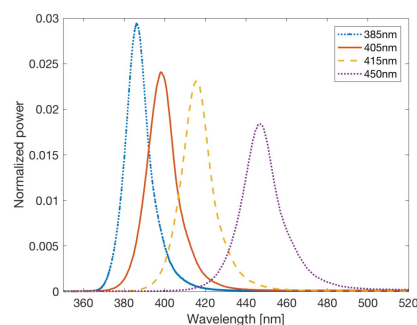


Fig. 1. Normalized SPD curves of four LEDs.

of the irradiance in the target spot from every light source was measured using a PM100D power meter with a S120VC probe (Thorlabs, Newton, NJ, USA). According to the measurements, the average irradiance in the central 6cm-diameter circle was 49.39 mW/cm², with a relative variation of only 6.56%. Therefore, the central light beam can be approximately regarded as being unidirectional; and the light source can be treated as a planar one. Thus, the measured irradiance and fluence rate are identical, both of which are numerically equal to the radiance in the direction of incidence of the photon beam [35].

4) Singlet Oxygen Assay: The SOSG reagent is highly selective for 1O_2 . Unlike other available fluorescent and chemiluminescent singlet oxygen detection reagents, it does not exhibit any appreciable response to hydroxyl radical or superoxide. Before the assay, the fungal suspension was first washed by phosphate buffer saline (PBS) for three times. The SOSG stock solution was then added to it in a ratio of 1:1000. Next, the suspension was seeded into a 96-well plate and was irradiated by one of the four LED light sources. The cell suspension in one well was resuspended and placed in the dark at each sampling point of 0, 5, 10, 15, 20, 25, and 30 min.

Immediately after the light treatment, the singlet oxygen concentration levels of the cell suspension were measured as fluorescent levels using a VL0L0TD0 Varioskan LUX microplate reader (Thermo Fisher, Waltham, MA, USA), with the excitation and emission wavelengths set at 488 nm and 525 nm, respectively.

It is worth mentioning here that two potential factors that could affect the accuracy of the assays were analyzed via preliminary experiments. Firstly, the temperature of the PBS solvent after being continuously irradiated for 30 min by the four light sources was measured, and was found to be lower than 37°C in all the four cases. This indicated that the light irradiation could not lead to a temperature that was prohibitive to the *C. albicans*. Secondly, the absorption of the light by the PBS solvent was evaluated. The experimental measurements indicated that this absorption was indeed negligible, because of the colorless and transparent nature of the solvent. Therefore, the influence of both the light-induced heat and the light absorption by the PBS solvent on the light-induced 1O_2 was negligible.

5) Statistics: In the ROS assays, the raw data were processed to produce the mean and standard deviation for each treatment time interval. The significance of ROS levels and

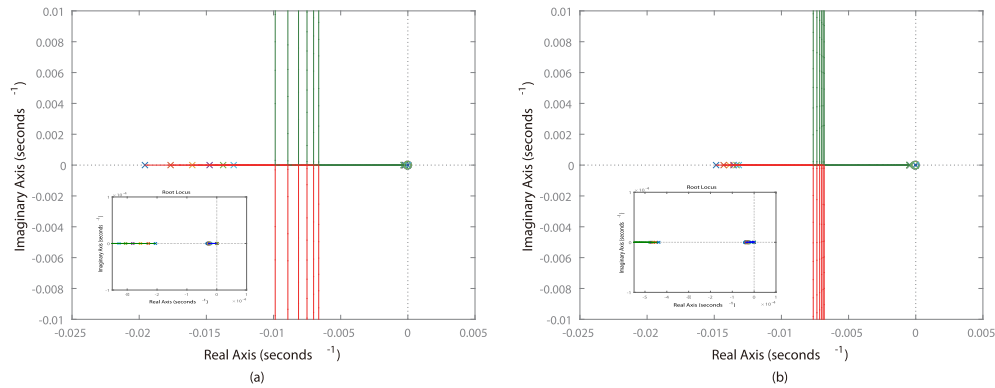


Fig. 2. The root locus plots of the seven linearized MSO processes at different equilibrium points: (a) $^3\text{O}_2$ deficient case, (b) $^3\text{O}_2$ rich case. The scales of the corresponding axes in the two figures are the same. The inserts in the figures show the cancellation of the pole $s = 0$ with the zero.

viability of cells were tested by the Student's t-test. The values of $P < 0.05$ were considered statistically significant.

III. RESULTS

A. Simulation Results

1) Simulation and Analysis of the First-Principle MSO Model: By taking the MSO model (1) as the first-principle model, we simulated the ODEs of the model using Runge-Kutta-Fehlberg (RK45) method. The parameters were taken from a photofrin-mediated PDT model [21], i.e., $\sigma = 9 \times 10^{-5} \mu\text{M}^{-1}$, $\xi = 3.7 \cdot 10^{-3} \text{cm}^2/\text{mW/s}$, $\delta = 33 \mu\text{M}$, and $\beta = 11.9 \mu\text{M}$. The irradiance was set as $\phi = 50 \text{mW/cm}^2$. For the case with deficient oxygen concentration, $[^3\text{O}_2]_0$ and the supply rate g were set as in the normal condition as $[^3\text{O}_2]_0 = 50 \mu\text{M}$, $g = 0.5 \mu\text{M/s}$. On the other hand, in the case of rich oxygen concentration, their values were respectively set as $[^3\text{O}_2]_0 = 80 \mu\text{M}$ and $g = 1 \mu\text{M/s}$, i.e., their maximum values mentioned in [21]. The irradiation time was set to 30 min with a step size of 5 min, which corresponded to the experimental time interval and total irradiation time.

In both cases, a sequence of time-series data with seven samples were generated, and were then taken as the equilibrium points to linearize the original nonlinear model (1). The root locus plots of these seven LTI systems are shown in Fig. 2. Two observations can be clearly made. First, the zero ranges from -5×10^{-5} to -2×10^{-5} , and cancels with the pole at the origin of all the seven LTI systems in both cases. Second, in the oxygen rich case, the root loci at the different points are condensed to a much smaller cluster, than those in the oxygen deficient case. This indicates that the LTI systems in the oxygen rich case are more identical to each other.

Then, the remaining two poles after the pole-zero cancellation were respectively calculated for both cases, and are shown in Fig. 3. Obviously, the variation of the poles in the oxygen deficient case is much larger than that in the oxygen rich case. Specifically, the magnitude of the non-dominant pole drops from 50.98 % to 12.85 %, when the oxygen concentration increases; while the drop in the dominant pole is even more remarkable, i.e., from 59.37 % to 9.14 %.

2) Validation of the Linearized Model (6) to Model (1) by Simulations: In this section, the linearized model (6) was used to simulate $[^1\text{O}_2]$ in an oxygen-rich environment. Because this

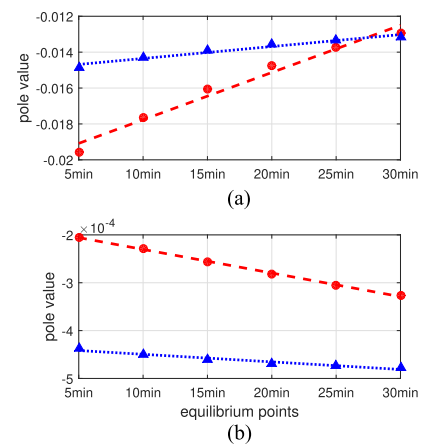


Fig. 3. The pole positions of the linearized MSO process at different equilibrium points: (a) non-dominant pole, (b) dominant pole. Circles: $^3\text{O}_2$ deficient case. Triangles: $^3\text{O}_2$ rich case.

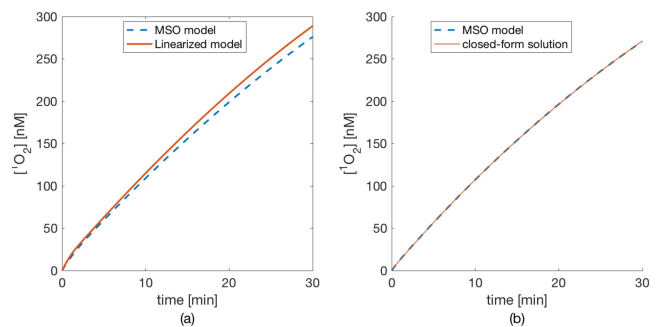


Fig. 4. The accuracy of the (a) linearized model and (b) closed-form solution comparing to the first-principle model.

system can be regarded as a linear system with an abundant oxygen supply, A and B were fixed to their mean value in (6). The fitting result is plotted in Fig. 4(a) with a 8.5366 average root mean square error (RMSE).

3) Validation of the Closed-Form Solution (18) to Model (1) by Simulations: In this section, the closed-form solution of the first-principle model was verified under different oxygen supplies. We first consider the situation of an ample oxygen supply. The oxygen-concentration related parameters were set

TABLE I
ESTIMATED PARAMETERS OF (18)

k_1	k_2	k_3	k_4	RMSE
6.289e+03	0.0920	7.168e-06	609.553	1.2087

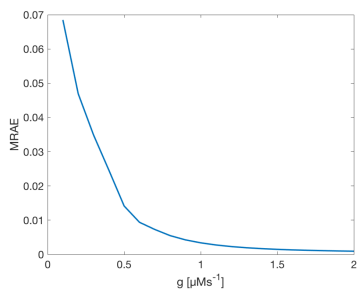


Fig. 5. The fitting accuracy of the closed-form solution (18) as compared to the first-principle model (1) in different oxygen supply rate g .

as $g = 0.8 \mu\text{M/s}$, $[^3\text{O}_2] = 50 \mu\text{M}$. The simulated results between the closed-form solution (18) and model (1) are shown in Fig. 4(b). The estimated parameters are shown in Table I. The RMSE of the fitted model (18) is only 1.2087, which obviously demonstrates its accuracy.

The entire simplification is based on the approximation of an abundant oxygen supply. Thus, we verified the closed-form solution (18) with different oxygen supply rates g . The Mean relative absolute errors (MRAE), defined as follows, of (18) compared to the first principle model with different oxygen supply rates are depicted in Fig. 5.

$$MRAE = \frac{1}{T} \sum_{t=1}^T \frac{|[\widehat{^1\text{O}_2}]_t - [^1\text{O}_2]_t|}{[^1\text{O}_2]_t} \quad (25)$$

The perfect fit of the closed-form solution (18) to the simulated data motivated us to fit the experimental data to this model.

B. Experimental Results

1) Measurements of the Singlet Oxygen Concentrations in *C. Albicans* At ABL Irradiation: The time sequences of the singlet oxygen concentrations in the *C. albicans* were measured from the experiments using all four different light sources, as shown in Fig. 6. The singlet oxygen concentration was significantly increased after 10 min irradiation of 385 nm wavelength ($P < 0.05$). In other cases, a significant increase in $[^1\text{O}_2]$ was observed within 5 min of irradiation ($P < 0.05$). The significance of the singlet oxygen concentration in fungi before and after the light treatment was tested by the Student's t-test.

2) Fitting the Parameters of (18) to the Experimental Data: Due to the aforementioned challenges in parameterizing the model of the induced $[^1\text{O}_2]$ in vitro, a closed-form solution of the MSO process was developed. One needs to estimate four parameters (k_1, k_2, k_3 , and k_4) to use this model. More specifically, k_1 and k_2 rely on the type of pathogen and its endogenous PS; k_4 is an offset to the initial concentration of singlet oxygen, whereas k_3 relies on the type of the pathogen and the PS, and also on the photochemical parameters that are related to the photon energy.

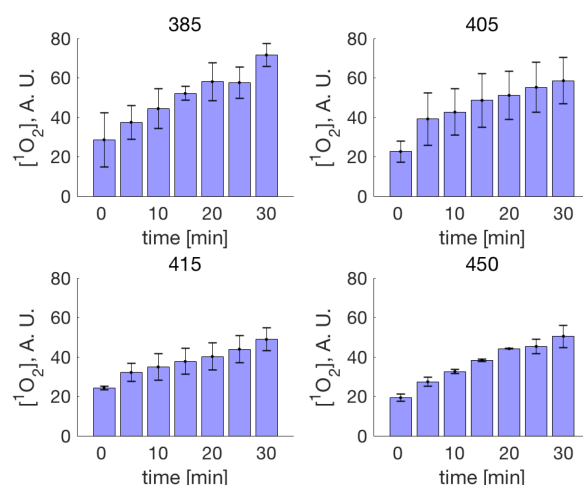


Fig. 6. The singlet oxygen concentration in *C. albicans* induced by different light wavelength.

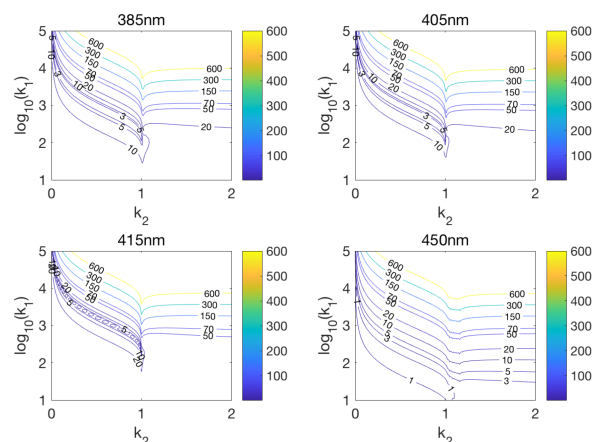


Fig. 7. The fitting errors with different values of k_1 and k_2 , where the numbers on the color bars and the contours are the MRAE errors.

Motivated by the definition of these parameters, we first fix the values of k_1, k_2 , and k_4 , and then built a functional relationship between k_3 and photon energy to investigate the light-induced $^1\text{O}_2$ of *C. albicans* by different light wavelengths.

First, a standard least-squares (LS) algorithm was used to coarsely tune the values of k_1, k_2, k_3 , and k_4 . The values of these parameters fitted to the experimental data with different wavelengths are listed in Table II. It is found that k_1 and k_2 were almost constant regardless of the wavelengths.

The MRAE errors for the values of k_1 and k_2 are shown in Fig. 7. It can be seen that in all the four cases, the optimum of the parameter pair (k_1, k_2) lies on the flat bottom of a narrow valley roughly within the range of $10 < k_1 < 10^4$ and $0.1 < k_2 < 1$. Thus, we set $k_1 = 280$ and $k_2 = 0.9$ as constant for all cases.

Second, with fixed k_1, k_2 , again, we used the LS algorithm to fine-tune k_3 and k_4 . The results are listed in Table III and plotted in Fig. 8. k_4 was found to be approximately constant in the results and can therefore also be fixed at $k_4 = 670$. In contrast, k_3 was sharply altered in different experiments.

In (18), k_3 determines the speed of generating $^1\text{O}_2$ in the photochemical reaction. The larger the value, the faster the accumulation of the cytotoxic $^1\text{O}_2$.

TABLE II
COARSELY TUNED VALUES OF THE PARAMETERS OF (18) BY LEAST SQUARES

Wavelength [nm]	k_1	k_2	k_3	k_4	RMSE
385	305.8660	0.8971	1.400e-5	716.1151	5.6245
405	257.9358	0.9399	8.000e-6	749.1535	4.3801
415	281.9836	0.9855	2.031e-06	1197.8264	1.5716
450	318.8462	0.7893	1.8e-5	517.9739	1.4840

TABLE III
FINE TUNED VALUES OF K3 AND K4 IN (18)

Wavelength [nm]	k_3	k_4	RMSE
385	1.1240e-05	674.6588	2.4744
405	9.0556e-06	673.8206	3.4526
415	6.0888e-06	671.0575	1.2636
450	8.5290e-06	666.1381	1.4852

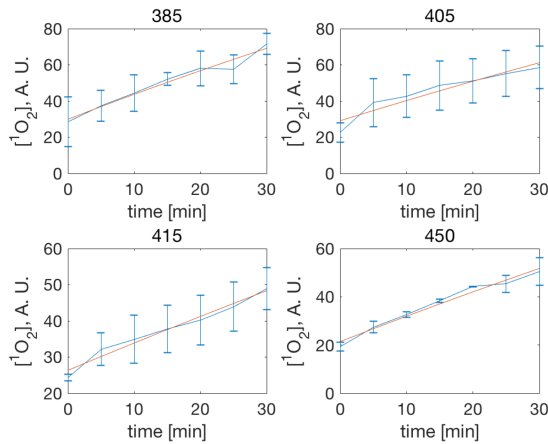


Fig. 8. Fitted curve to the measured $[^1O_2]$ from different wavelength light irradiation experiment.

3) Relationship Between k_3 and Photon Energy: To fit and validate the relationship between k_3 and photon energy, we split the experimental data into two groups, i.e., with those from the 385 nm, 405 nm, and 450 nm light experiments for fitting, and with the 415 nm experimental data for validation.

In (20), there are totally nine unknown parameters to be estimated, i.e., a_1 , a_2 , b_1 , b_2 , c_1 , c_2 , d_1 , d_2 , and E . However, there are only three data points, which are not enough to uniquely determine all these nine parameters by solving a single LS problem. To fit them, c_1 and c_2 were first determined by estimating the periods of the sinusoidal functions. More specifically, c_1 was greater than c_2 which corresponds to the PS of the *C. albicans* absorption spectra. Then, b_1 and b_2 were secondly estimated by the heights of the peaks. For the same reason, b_1 is smaller than b_2 . This then reduces the number of unknown parameters to five, where a_1 , a_2 , d_1 and d_2 can now be estimated by a nonlinear LS algorithm with reasonable accuracy; and \bar{E} is finally determined by the intersection of piecewise functions. As a result, the value of k_3 in the fitted model at 415 nm turned out to be 5.855×10^{-6} which is plotted on Fig. 9. As a validation, the fitted k_3 by the experimental data was 6.089×10^{-6} as reported in Table III. The difference between the model output and the

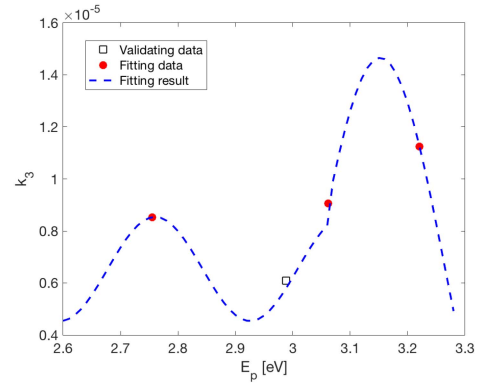


Fig. 9. Fitted model of k_3 as a function of the photon energy.

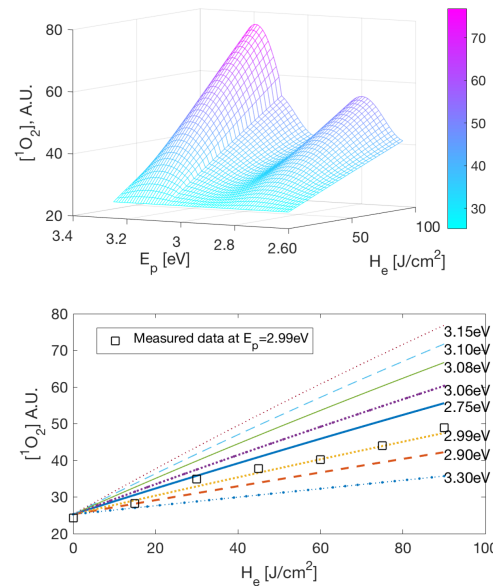


Fig. 10. $[^1O_2]$ in response to various photon energy and fluence rate, where the numbers on the color bar indicate the values of $[^1O_2]$.

experimentally fitted k_3 at this validation point was about 4%, which is acceptable.

4) Modeling Singlet Oxygen as a Function of Photon Energy and Fluence Rate: With the parameters in Table IV on page 9, the model of $[^1O_2]$ as a function of the stimulating photon energy and fluence rate, i.e., (21), was finally established, with the validation using the 415 nm ($E_p = 2.99$ eV) experimental data. The simulation results are plotted in Fig. 10 where the validating data are shown in squares. The RMSE error of the predicted $[^1O_2]$ from the model compared to the validating

TABLE IV
ESTIMATION OF THE PARAMETERS OF (21)

a_1	a_2	b_1	b_2	c_1	c_2	d_1	d_2	k_1	k_2	k_4
6.655e-06	6.537e-6	8e-6	2e-6	14	19	0.999	0.960	280	0.9	670

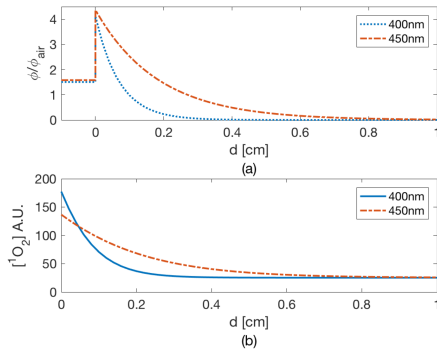


Fig. 11. The spatial distributions of (a) fluence rate and (b) 1O_2 concentration up to 1 cm depth within human epidermis.

experimental measurements was only 1.251. Therefore, the accuracy of this model at the validation point is also acceptable. However, the limitation of this model is that it is accurate only in an oxygen-rich environment. According to our simulation studies, a rule of thumb to determine the richness of oxygen supply is that the supply rate shall be higher than $0.4 \mu\text{Ms}^{-1}$ for *in vivo* or clinical experiments.

From the simulation results of (21), the following observations can be further made. First, when the fluence rate is low, i.e., $H_e < 5 \text{ J/cm}^2$, 1O_2 is insufficiently induced by any photon energy in the range of $2.6 \sim 3.2 \text{ eV}$. This indicates that sufficiently large radiometric energy of the stimulating light is required to trigger sufficient singlet oxygen generation, no matter how large the photon energy is. Second, as the fluence rate accumulates to a certain level, i.e., $H_e > 15 \text{ J/cm}^2$, the photon energy becomes the main factor to determine $[^1O_2]$. For the fungi studied in this study, *C. albicans*, the photon energy in the range of either $2.7 \sim 2.8 \text{ eV}$ or $3.0 \sim 3.2 \text{ eV}$ ($388 \sim 413 \text{ nm}$ or $443 \sim 459 \text{ nm}$ in wavelength) can more effectively stimulate singlet oxygen generation, which coincides with the Sorét bands of common types of porphyrin and flavin.

5) Quantifying the Fluence Rate for Treating Fungal Infections in Cutaneous Tissues: To study the clinical effect of ABL on treating superficial infections, knowing the fluence rate delivered to the tissues beneath the surface is important. To this end, we first collected the optical properties of healthy human epidermis from the literature, including the absorption coefficient μ_a and the reduced scattering coefficient μ'_s . Due to the limited measurements reported so far, it was still not possible to find all the values exactly corresponding to the four wavelengths. Fortunately, in the studied range of wavelength, the available values were found to be $\mu_a = 1.5 \text{ cm}^{-1}$, $\mu'_s = 10 \text{ cm}^{-1}$ at 400 nm, and $\mu_a = 1 \text{ cm}^{-1}$, $\mu'_s = 9 \text{ cm}^{-1}$ at 450 nm [36]. By respectively applying these parameters in Eqs. (22–24), we simulated the light fluence rate up to 1 cm depth beneath the epidermis. The result is shown in Fig. 11(a). As can

be seen, the light fluence rate increases sharply at the air-tissue boundary because of the backscattering from the boundary; and then exponentially decreases with the increasing depth. More specifically, the fluence rate of the 400 nm light decreases faster than that of the 450 nm. For instance, the fluence rate of 450 nm at 0.2 cm depth is 5.5 times larger than that of 400 nm. That is to say, the 450 nm can penetrate deeper than 400 nm.

Furthermore, the spatial distribution of the induced 1O_2 concentration was simulated using (21), with a total fluence rate of 90 J/cm^2 . The simulation result is shown in Fig. 11(b), where the 1O_2 concentration exponentially decreases with the increasing depth.

IV. DISCUSSION

A. Conditions and Accuracy of the Linearized Model (6)

According to both the root loci in Fig. 2 and the pole positions in Fig. 3, the nonlinearity of the MSO process (1) is greatly reduced in an oxygen rich environment. The process can thus be approximately treated as linear. It is worth mentioning that it is much easier for such a linear model to be obtained from the first-principle model or identified from time-series data. On the other hand, the dominant poles λ_2 of the oxygen rich case are faster than their counterparts in the oxygen deficient case. This also indicates that the response of 1O_2 to light stimulation is faster, when the main ingredient 3O_2 is abundant.

More specifically, as analyzed in (12), when the concentration of triplet oxygen $[^3O_2]$ is far greater than β , $[S_0]$ will become the only time-varying parameter that can change the pole. In the simulation, although $[^3O_2]$ is not infinite, it is still approximately five times more than β with a normal oxygen content environment; this ratio increases to ten times greater in an oxygen-rich environment. Thus, $[S_0]$ is the main factor that determines the pole positions in an oxygen-rich environment. Moreover, since σ is far less than the other parameters in (1), i.e., $\sigma = 9 \cdot 10^{-5} \mu\text{M}^{-1}$, $\xi = 3.7 \cdot 10^{-3} \text{ cm}^2/\text{mW/s}$, $\delta = 33 \mu\text{M}$, $\beta = 11.9 \mu\text{M}$, the variation of $[S_0]$ is relatively lower than that of the other components. In the simulation, $\frac{d[S_0]}{dt}$ was only about 1% of $\frac{d[^3O_2]}{dt}$ and $\frac{d[^1O_2]}{dt}$ in the entire process. Therefore, there was little change in the pole positions over time in the oxygen-rich environment, and thus, the dynamics could be approximated to those of a linear system. This provides the insight into the dynamic behavior of the MSO process, in the sense that the MSO process is approximately linear in the presence of ample oxygen concentration.

For a linear system, a linearized model (6) was used to simulate the changes in 1O_2 . However, the fitting results were suboptimal as compared to using the nonlinear model (18). The reason for this can be the nonlinearity of the MSO model. As we previously discussed, the MSO model can be approximated to linear in an oxygen-rich environment. However, the poles

are slowly changing over time, and strictly speaking, it remains a nonlinear model. This causes error in the linearized model, which assumes the fixed system poles and zeros.

B. Conditions and Accuracy of the Model (18)

The closed-form solution is based on the condition of abundant oxygen supply. The concentration of 3O_2 was assumed to be infinite in the derivation of (18). Although $[{}^3O_2]$ cannot be infinite in reality, when the value of $[{}^3O_2]$ is sufficiently large, the accuracy of the closed-form solution is acceptable. In Fig. 5, we validated this solution under different oxygen supply rates. More specifically, when the oxygen supply rate $g > 0.4 \mu M s^{-1}$, the MRAE of (18) is always higher than 98%. When $g = 0.8 \mu M s^{-1}$, shown in Fig. 4(b), the accuracy of the closed-form solution can be up to 99%. In reality, the oxygen supply rate in human tissues is in the range of $0.1 - 1 \mu M s^{-1}$ [21]. Therefore, in most cases, this simplified closed-form model can still give accurate enough results.

It shall be mentioned that knowing the level of oxygen during PDTs is also important to predict the PDT efficacy [37], since the cytotoxic effect of PDTs depends in part on the availability of molecular oxygen in the target tissue. In this aspect, it was reported that high fluence rates could lead to a reduced photodynamic effect due to the oxygen depletion [38]. Therefore, for the accuracy of our model, it shall also be recommended to avoid apply high fluence rates in clinical treatment. On the other hand, applying a pulsed light with high amplitude can also be a way out. To determine the optimum timing of the duty cycles of the light pulses, a mathematical model can be used to analyze their effects on intercapillary tissue during PDTs [39].

On the other hand, it shall also be noted that the accuracy of the closed-form MSO model is dependent on the oxygen supply rate g . According to our simulation studies, a rule of thumb to determine the richness of oxygen supply is that the supply rate shall be higher than $0.4 \mu M s^{-1}$. In reality, g also depends on blood flow rate; and $g = 0.7 \mu M s^{-1}$ is a well-accepted value in PDTs [22], [40], which clearly meets the condition of an accurate closed-form MSO model. Besides, in treating superficial infection, due to the direct exposure of the treatment area to the air, the oxygen supply can be even higher. Therefore, the oxygen-rich environment assumption can be satisfied in both cases, and does not impose any limitation to apply the model.

C. Clinical Relevance of the Closed-Form Model (18)

In traditional PDTs, reduced tumor sizes and cure index are usually considered as their outcomes, which have been found to be highly correlated with the concentration of singlet oxygen [22], [24]. Therefore, the first principle model (1) is widely applied clinically to determine the specified light dosage with a target $[{}^1O_2]$. Since the closed-form MSO model (18) is directly derived from (1), it can be equivalently used to evaluate the PDT outcomes, under the aforementioned condition of ample oxygen supply.

It shall be emphasized that although (18) was especially tested in treating fungal infections, this model can actually be applied to all cases of antimicrobial light therapies and PDTs. In any case,

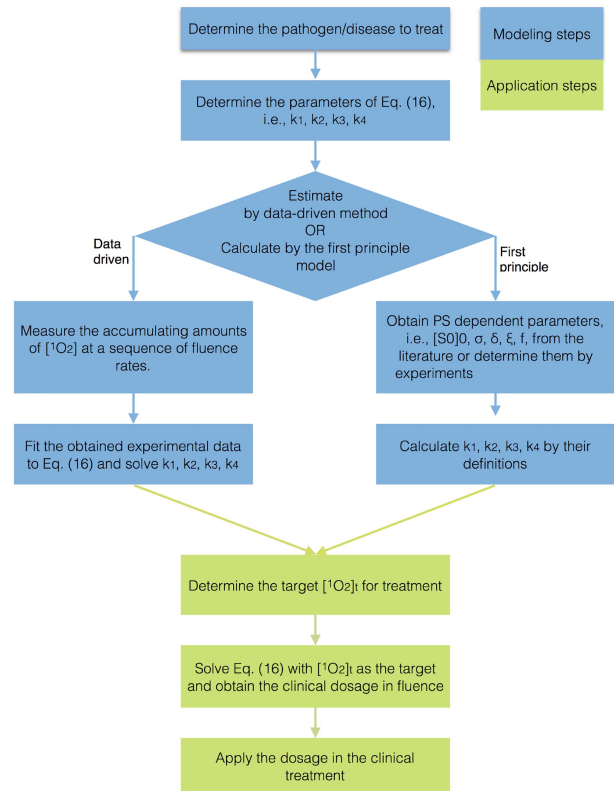


Fig. 12. Procedures in applying the closed-form algebraic model (18).

one only needs to estimate the four parameters (k_1, k_2, k_3 and k_4) to establish the model. To this end, a data-driven method was used in Section III-B2 to estimate them. On the other hand, these parameters can also be calculated with the knowledge of the PS dependent parameters, i.e., $[S_0]_0, \sigma, \delta, \xi$ and f . These parameters can be obtained either from the relevant literature or by conducting experiments following standard procedures [23]. Once $k_1 \sim k_4$ are determined, $[{}^1O_2]$ can be calculated with a specified fluence by (18). The 1O_2 concentration can then be used to predict the PDT outcomes. In traditional PDTs, the relationship between the 1O_2 concentration and treatment outcome can be found in many literatures. For instance, when $[{}^1O_2] > 1.1 mM$, the radiation-induced fibrosarcoma tumors exhibited a complete response after 14 days PDT treatment [40]. For the more susceptible bacteria, it was reported that *S. typhimurium* and *E. coli* were inactivated by 99% with $[{}^1O_2]$ accumulated to $74 \mu M$ [41]. As a summary, the procedures of establishing the model (18) for a potential clinical application are illustrated in Fig. 12.

V. CONCLUSION

In this work, the nonlinearity of the MSO process was examined by the poles of its linearized models at different equilibrium points. It was found that this system is linear in an oxygen-rich environment. Thus, the MSO model can be reduced to a linear dynamic model. Although this linearized model provides additional insights into the dynamic behavior of the MSO process, it can also lead to approximation errors in the prediction of long-time trajectories. Hence, an closed-form exact solution of

MSO model was derived. Furthermore, based on this analytical solution, a general model was developed as a function of the photon energy and light fluence rate.

We also measured the singlet oxygen concentration of *C. albicans* up to 30 min with the irradiation of 385, 405, 415, and 450 nm light. The fitting results of our model are in agreement with the experimental data, indicating the effectiveness of the proposed model and parameter estimation methods. We discovered that the photon energy within the range of 2.7 ~ 2.8 eV or 3.0 ~ 3.2 eV (388 ~ 413 nm or 443 ~ 459 nm in wavelength) is more effective in generating singlet oxygen in the fungi studied in this work, and is hence more effective in treating the infections caused by this type of fungi.

A potential extension of the current work is to model and compare the light induced singlet oxygen in other types of infectious fungal strains based on the developed analysis and modeling methods.

ACKNOWLEDGMENT

The authors would like to thank the anonymous reviewers for the greatly detailed and helpful comments.

REFERENCES

- [1] T. J. Dougherty *et al.*, "Photodynamic therapy," *J. Nat. Cancer Inst.*, vol. 90, no. 12, pp. 889–905, 1998.
- [2] T. Maisch, "A new strategy to destroy antibiotic resistant microorganisms: Antimicrobial photodynamic treatment," *Mini Rev. Med. Chem.*, vol. 9, no. 8, pp. 974–983, 2009.
- [3] T. Dai *et al.*, "Blue light for infectious diseases: Propionibacterium acnes, helicobacter pylori, and beyond?," *Drug Resist. Updates*, vol. 15, no. 4, pp. 223–236, 2012.
- [4] J. S. Guffey *et al.*, "Inactivation of mycobacterium smegmatis following exposure to 405-nanometer light from a supraluminous diode array," *Wounds*, vol. 25, no. 5, pp. 131–135, 2013.
- [5] M. Dring, "Photocontrol of development in algae," *Annu. Rev. Plant Physiol. Plant Mol. Biol.*, vol. 39, no. 1, pp. 157–174, 1988.
- [6] Y. Zhang *et al.*, "Antimicrobial blue light inactivation of candida albicans: In vitro and in vivo studies," *Virulence*, vol. 7, no. 5, pp. 536–545, 2016.
- [7] F. Halstead *et al.*, "Violet-blue light arrays at 405 nanometers exert enhanced antimicrobial activity for photodisinfection of monomicrobial nosocomial biofilms," *Appl. Environ. Microbiol.*, vol. 85, no. 21, 2019, Art. no. e01346-19.
- [8] R. Yin *et al.*, "Light based anti-infectives: Ultraviolet c irradiation, photodynamic therapy, blue light, and beyond," *Curr. Opin. Pharmacol.*, vol. 13, no. 5, pp. 731–762, 2013.
- [9] R. R. Allison and K. Moghissi, "Photodynamic therapy (PDT): PDT mechanisms," *Clin. Endoscopy*, vol. 46, no. 1, pp. 24–29, 2013.
- [10] M. Hayyan *et al.*, "Superoxide ion: Generation and chemical implications," *Chem. Rev.*, vol. 116, no. 5, pp. 3029–3085, 2016.
- [11] G. Pannov *et al.*, "The role of iron in N_2O decomposition on ZSM-5 zeolite and reactivity of the surface oxygen formed," *J. Mol. Catalysis*, vol. 61, no. 1, pp. 85–97, 1990.
- [12] J.-P. Pouget *et al.*, "DNA damage induced in cells by γ and UVA radiation as measured by HPLC/GC-MS and HPLC-EC and comet assay," *Chem. Res. Toxicol.*, vol. 13, no. 7, pp. 541–549, 2000.
- [13] J. F. Turrens, "Mitochondrial formation of reactive oxygen species," *J. Physiol.*, vol. 552, no. 2, pp. 335–344, 2003.
- [14] T. C. Zhu and J. C. Finlay, "The role of photodynamic therapy (PDT) physics," *Med. Phys.*, vol. 35, no. 7, pp. 3127–3136, 2008.
- [15] A. E. Profio and D. R. Doiron, "Dosimetry considerations in phototherapy," *Med. Phys.*, vol. 8, no. 2, pp. 190–196, 1981.
- [16] J. Dysart *et al.*, "Sci-YIS Fri-03: Calculation of singlet oxygen dose from photosensitizer photobleaching during MTHPC or photofrin photodynamic therapy in vitro," *Med. Phys.*, vol. 32, no. 7, pp. 2419–2419, 2005.
- [17] I. Georgakoudi *et al.*, "The mechanism of photofrin photobleaching and its consequences for photodynamic dosimetry," *Photochemistry Photobiol.*, vol. 65, no. 1, pp. 135–144, 1997.
- [18] X.-H. Hu *et al.*, "Modeling of a type II photofrin-mediated photodynamic therapy process in a heterogeneous tissue phantom," *Photochemistry Photobiol.*, vol. 81, no. 6, pp. 1460–1468, 2005.
- [19] T. C. Zhu *et al.*, "Macroscopic modeling of the singlet oxygen production during PDT," *Proc. SPIE*, vol. 6427, 2007, Art. no. 642708.
- [20] K. W. Beeson *et al.*, "Validation of combined monte carlo and photokinetic simulations for the outcome correlation analysis of benzoporphyrin derivative-mediated photodynamic therapy on mice," *J. Biomed. Opt.*, vol. 24, no. 3, 2019, Art. no. 035006.
- [21] G. Kareliotis, S. Liossi, and M. Makropoulou, "Assessment of singlet oxygen dosimetry concepts in photodynamic therapy through computational modeling," *Photodiagnosis Photodynamic Ther.*, vol. 21, pp. 224–233, 2018.
- [22] K. K.-H. Wang *et al.*, "Explicit dosimetry for photodynamic therapy: Macroscopic singlet oxygen modeling," *J. Biophotonics*, vol. 3, no. 5-6, pp. 304–318, 2010.
- [23] M. M. Kim *et al.*, "On the in-vivo photochemical rate parameters for PDT reactive oxygen species modeling," *Phys. Med. Biol.*, vol. 62, no. 5, pp. R1–R48, 2017.
- [24] T. Sheng *et al.*, "Reactive oxygen species explicit dosimetry to predict local tumor growth for photofrin-mediated photodynamic therapy," *Biomed. Opt. Exp.*, vol. 11, no. 8, pp. 4586–4601, 2020.
- [25] Y. Gu *et al.*, "Nonlinear modeling of cortical responses to mechanical wrist perturbations using the NARMAX method," *IEEE Trans. Biomed. Eng.*, vol. 68, no. 3, pp. 948–958, Mar. 2021.
- [26] J. Dong and T. Wang, "Data driven modeling of the reactive oxygen species stimulated by photon energy in light therapies," *IEEE Access*, vol. 8, pp. 18196–18206, 2020.
- [27] T. Wang *et al.*, "Analyzing efficacy and safety of anti-fungal blue light therapy via kernel-based modeling the reactive oxygen species induced by light," *IEEE Trans. Biomed. Eng.*, vol. 69, no. 8, pp. 2433–2442, Aug. 2022.
- [28] R. A. Calderone and W. A. Fonzi, "Virulence factors of candida albicans," *Trends Microbiol.*, vol. 9, no. 7, pp. 327–335, 2001.
- [29] T. Arendorf and D. Walker, "The prevalence and intra-oral distribution of Candida albicans in man," *Arch. Oral Biol.*, vol. 25, no. 1, pp. 1–10, 1980.
- [30] J. D. Sobel, "Vaginitis," *New England J. Med.*, vol. 337, no. 26, pp. 1896–1903, 1997.
- [31] R. C. Dorf and R. H. Bishop, *Modern Control Systems*. Upper Saddle River, NJ, USA: Pearson Prentice Hall, 2008.
- [32] A. Dimofte *et al.*, "In vivo light dosimetry for motexafin lutetium-mediated PDT of recurrent breast cancer," *Lasers Surg. Med.*, vol. 31, no. 5, pp. 305–312, 2002.
- [33] J. L. Sandell and T. C. Zhu, "A review of in-vivo optical properties of human tissues and its impact on PDT," *J. Biophotonics*, vol. 4, no. 11-12, pp. 773–787, 2011.
- [34] S. L. Jacques, "Light distributions from point, line and plane sources for photochemical reactions and fluorescence in turbid biological tissues," *Photochemistry Photobiol.*, vol. 67, no. 1, pp. 23–32, 1998.
- [35] T. C. Zhu *et al.*, "Absolute calibration of optical power for PDT: Report of AAPM TG140," *Med. Phys.*, vol. 40, no. 8, 2013, Art. no. 081501.
- [36] E. V. Salomatina *et al.*, "Optical properties of normal and cancerous human skin in the visible and near-infrared spectral range," *J. Biomed. Opt.*, vol. 11, no. 6, 2006, Art. no. 064026.
- [37] J. Moan and S. Sommer, "Oxygen dependence of the photosensitizing effect of hematoporphyrin derivative in nhik 3025 cells," *Cancer Res.*, vol. 45, no. 4, pp. 1608–1610, 1985.
- [38] T. H. Foster *et al.*, "Oxygen consumption and diffusion effects in photodynamic therapy," *Radiat. Res.*, vol. 126, no. 3, pp. 296–303, 1991.
- [39] J. P. Henning *et al.*, "A transient mathematical model of oxygen depletion during photodynamic therapy," *Radiat. Res.*, vol. 142, no. 2, pp. 221–226, 1995.
- [40] H. Qiu *et al.*, "A comparison of dose metrics to predict local tumor control for photofrin-mediated photodynamic therapy," *Photochemistry Photobiol.*, vol. 93, no. 4, pp. 1115–1122, 2017.
- [41] T. A. Dahl *et al.*, "Comparison of killing of gram-negative and gram-positive bacteria by pure singlet oxygen," *J. Bacteriol.*, vol. 171, no. 4, pp. 2188–2194, 1989.